Journal of Colloid and Interface Science 670 (2024) 124–131

Contents lists available at ScienceDirect

Journal of Colloid And Interface Science

journal homepage: www.elsevier.com/locate/jcis

Regular Article

Fine-tuning nanoflower-like Fe/Co hybrids with high content oxyhydroxide accelerating oxygen evolution kinetics

Lixia Wang [a,1], Jia Huang [a,1], Qiuping Gan [a], Jiasui Huang [a], Xinran Hu [a], Dongcheng Liu [a,*], Tayirjan Taylor Isimjan [b,*], Xiulin Yang [a,*]

[a] Guangxi Key Laboratory of Low Carbon Energy Materials, School of Chemistry and Pharmaceutical Sciences, Guangxi Normal University, Guilin 541004, China
[b] Saudi Arabia Basic Industries Corporation (SABIC) at King Abdullah University of Science and Technology (KAUST), Thuwal 23955-6900, Saudi Arabia

HIGHLIGHTS

- A nanoflower-like FeCo hybrids is synthesized by a facile electrodeposition method.
- The Fe_9-Co_1 catalyst delivers a good OER activity (η_{50} = 222 mV) and stability.
- The reconstructed FeOOH/CoOOH serves as the real active sites during OER process.
- The synergy between Co and Fe species reduces the activation energies with intermediates and improves OER activity.

GRAPHICAL ABSTRACT

ARTICLE INFO

Keywords:
Electrodeposition
Oxygen evolution reaction
Electrocatalyst
Overall water splitting

ABSTRACT

Iron hydroxide (FeOOH) is a potential active component in iron-based electrocatalysts for water electrolysis. However, its catalytic performance is constrained by its slow oxygen evolution reaction (OER) kinetics. Herein, we synthesized a nanoflower-like FeCo-hydro(oxy)oxides composite with tunable Fe/Co ratios (Fe_x-Co_y) on nickel foam (NF) via a one-step electrodeposition technique. This method allows for precise control over the morphology and composition of the hybrid nanoflowers. The optimized Fe_9-Co_1 discloses favorable OER performance with a low overpotential of 222 mV at 50 mA cm^{-2} and demonstrates good stability exceeding 60 h at 10 mA cm^{-2}. Further, an assembled Fe_9-$Co_1^{(+)}$||$Pt/C^{(-)}$ dual-electrode configuration achieves a low cell voltage of 1.73 V at the current density of 100 mA cm^{-2} for water splitting, with long-term stability for 70 h and minimal degradation. Studies indicate that the distinctive nanoflower morphology of Fe_9-Co_1 enhances active site exposure, while both FeOOH and reconstructed CoOOH serve as catalytic centers, contributing to the observed OER performance. This work introduces a facile approach for synthesizing OER electrocatalysts, underscoring the role of the high-valence state of Fe/Co as active sites in the OER process.

* Corresponding authors.
E-mail addresses: ldcheng@gxnu.edu.cn (D. Liu), isimjant@sabic.com (T. Taylor Isimjan), xlyang@gxnu.edu.cn (X. Yang).
[1] These authors contributed equally to this work.

https://doi.org/10.1016/j.jcis.2024.05.034
Received 29 January 2024; Received in revised form 1 May 2024; Accepted 6 May 2024
Available online 12 May 2024

1. Introduction

The oxygen evolution reaction (OER) plays a pivotal role as a half-reaction in energy conversion and storage systems that rely on overall water splitting (OWS) [1,2]. The kinetics of OER are inherently sluggish due to the complex interplay of multiple proton-coupled electron transfer steps, posing a significant bottleneck in OWS efficiency [3–5]. IrO_2 and RuO_2 are currently among the most active OER electrocatalysts [6,7]. However, their exorbitant cost and limited stability hinder widespread applications [8]. Consequently, it is imperative to explore simple and rapid synthesis strategies for developing OER catalysts with high performance and enduring durability.

Transition metal hydroxides are considered promising OER electrocatalysts due to their numerous electrochemically active sites, rapid electron transport, and stability in alkaline electrolyte [9]. Recent studies indicate that numerous OER catalysts undergo dynamic and irreversible reconstruction in alkaline media, evolving into metal (oxy) hydroxides (M−OOH) as the authentic OER active species [10,11]. The environmentally friendly FeOOH has garnered attention as a potential OER catalyst [12]. However, pure FeOOH often exhibits poor electronic conductivity and limited OER activity [13–15]. Integrating hybrid materials with strong interaction effects between different components is an effective approach to enhance overall electrocatalytic activity. Consequently, synergistically incorporating FeOOH with other materials has proven effective in enhancing its activity [16]. Transition metal hydroxides, renowned for their distinctive structure, electronic properties, and inherent characteristics, offer possibilities for efficient OWS [17,18]. Extensive research has revealed that $Co(OH)_2$ undergoes spontaneous surface reconstruction, resulting in the formation of amorphous high-valent cobalt active layer structures during the OER process [19]. These structures have been identified as significant contributors to catalytic activity [20]. For instance, Zhou and colleagues engineered OER catalysts by fabricating amorphous bimetallic FeOOH/$Co(OH)_2$ heterostructured microchip arrays via a facile mechanical stirring strategy [21]. Wang et al. synthesized flower-like α-$Co(OH)_2$ with two-dimensional curled nanosheets, facilitating OH* and OOH* formation [22]. Therefore, composites of FeOOH and $Co(OH)_2$ offer an effective approach to achieve balanced adsorption/desorption processes and exploit synergistic effects between metals, potentially enhancing OER activity [23]. Additionally, among various morphologies, nanoflowers show potential in increasing active sites and expediting electron transfer, thereby elevating OER performance [24]. However, the catalysts are susceptible to agglomeration during prolonged synthesis procedures, resulting in reduced dispersion of dopant metals and active sites [25].

Herein, we present a rapid one-step electrodeposition strategyfor synthesizing a series of nanoflower-shaped Fe_x-Co_y hydro(oxy)oxides catalysts on nickel foam (NF) substrate. The Fe_9-Co_1 with an optimal Fe/Co ratio, exhibits catalytic activity for OER in alkaline media, requiring only a small overpotential of 222 mV to achieve a current density of 50 mA cm^{-2}, surpassing the benchmark RuO_2 catalyst. Intriguingly, a dual-electrode device composed of Fe_9-Co_1 and Pt/C achieves a current density of 100 mA cm^{-2} at an ultra-low voltage of 1.73 V, comparable to $RuO_2^{(+)}||Pt/C^{(-)}$. Furthermore, Fe_9-$Co_1^{(+)}||Pt/C^{(-)}$ exhibits long-term operational stability. The nanoflower architecture exposes more active sites, synergistic effects between iron and cobalt species, and a higher electrochemically active surface area are likely factors contributing to the improved OER catalytic performance of Fe_9-Co_1.

2. Experimental section

2.1. Chemicals and reagents

Iron sulfate heptahydrate ($FeSO_4·7H_2O$, 99.0~101.0%), cobalt (II) nitrate hexahydrate ($Co(NO_3)_2·6H_2O$, 99%), and ruthenium chloride ($RuCl_3$) were purchased from Inno-chem. Potassium hydroxide (KOH, 99.0%) was obtained from Guangxi Zoey Biotechnology Co., Ltd. Sulfuric acid (H_2SO_4, 95.0~98.0 %) and absolute ethanol (C_2H_5OH, ≥99.7%) were acquired from Xilong Science Co., Ltd. Commercial Pt/C (20 wt% Pt) and Nafion solution (5 wt%) were purchased from Alfa Aesar. Ni foam (NF) was purchased from Suzhou Sinero Technology Co., Ltd. All the reagents were analytical reagent and used without further purification.

2.2. Synthesis of Fe species on NF

Fe species were electrodeposited onto the NF substrate using a standard electrodeposition process. In the three-electrode deposition setup, a clean NF (1 × 1 cm^2) acted as the working electrode, while Pt foil and a saturated calomel electrode (SCE) served as the counter and reference electrodes, respectively. The electrodeposition technique used a 40 mL solution of 0.1 mol L^{-1} $FeSO_4·7H_2O$ as the electrolyte. The electrodeposition was conducted for 10 min at a current density of 10 mA, utilizing the Biologic VMP3 electrochemical station. Subsequently, the resulting NF was meticulously cleaned with deionized water and air-dried at room temperature. Similarly, deposition processes were performed for 5, 20, and 30 min, yielding samples denoted as Fe-5/NF, Fe-10/NF, Fe-20/NF, and Fe-30/NF.

2.3. Synthesis of Fe-Co species on NF

Fe-Co species with varying Fe/Co ratios were synthesized on NF by adjusting the ratios of $FeSO_4$ and $Co(NO_3)_2$ in the electrolyte (10:0, 9.5:0.5, 9:1, 8:2, 4:6, and 0:10) at a total metal salt concentration of 0.1 mol L^{-1}, labeled as Fe/NF, $Fe_{9.5}$-$Co_{0.5}$/NF, Fe_9-Co_1/NF, Fe_8-Co_2/NF, Fe_4-Co_6/NF and Co/NF, respectively. The synthetic process is the same as for producing Fe species on NF, with a 10-min electrodeposition time.

2.4. Synthesis of RuO_2

Ruthenium chloride solid was finely ground in a mortar and thoroughly mixed. The resulting powder was then annealed in air at 400 °C for 3 h to obtain RuO_2.

2.5. Materials characterization

The composition of all samples was determined using X-ray diffraction (XRD) analysis with a Rigaku D/Max X-ray diffractometer employing Cu Kα radiation. Scanning electron microscopy (SEM, Quanta FEG 200, Holland) and transmission electron microscopy (TEM, Talos F200S) were employed to assess the morphology of the electrocatalysts. Additionally, energy-dispersive X-ray (EDX) spectroscopy was used for compositional analysis. Inductively coupled plasma mass spectrometry (ICP-MS) using a PerkinElmer Corporation FLexar-NexION300X instrument provided a highly precise determination of the metal content in the various catalysts. X-ray photoelectron spectroscopy (XPS) analysis with a JPS-9010 TR Photo-electron Spectrometer from Japan was used to investigate the elemental composition and surface valence states of the materials. To ensure data accuracy and reproducibility, multiple analyses were performed using techniques such as XPS, ICP-MS, XRD, and others.

2.6. Electrochemical measurement

All electrochemical tests of the prepared catalysts were conducted using a Bio-logic VMP3 electrochemical workstation, employing a conventional three-electrode setup in a 1.0 M KOH solution. In this setup, the catalyst served as the working electrode, a graphite plate was used as the auxiliary electrode, and a saturated calomel electrode (SCE) served as the reference electrode. The prepared catalysts underwent electrochemical activation through cyclic voltammetry (CV) with 5 cycles at a scanning rate of 5 mV s^{-1} to reach a stable state. To assess the

performance of the catalysts in the oxygen evolution reaction (OER), polarization curves were obtained through linear sweep voltammetry (LSV) measurements at scan rates of 0.2 mV s^{-1}. Electrochemical impedance spectroscopy (EIS) was carried out by varying the scanning frequency from 2×10^{5} Hz to 10^{-2} Hz at 0.4 V. Furthermore, the electrochemically active surface area (ECSA) calculation based on double-layer capacitance (C_{dl}) values was evaluated using cyclic voltammetry (CV) at different scan rates. Chronoamperometry was employed to evaluate the catalyst's durability and long-term stability. The thermodynamic potential of 1.0 M KOH with H_2-saturated for approximately 30 min was determined by performing cyclic voltammetry (CV) at a scan rate of 5 mV s^{-1}. The average of the two potentials at the zero-crossing (1.039 V) of the current was calculated (Fig. S1). As a result, all the curves presented in this study were adjusted for *iR* compensation. Furthermore, all electrochemical tests were carried out at room temperature (25±1 °C). To eliminate any uncertainties and biases, the electrochemical performance data underwent over three replicate experiments.

3. Results and discussion

3.1. Synthesis and structural analysis

As depicted in Scheme 1, the Fe_x-Co_y/NF catalysts with varying Fe/Co molar ratios (x+y=0.1 mol L^{-1}) were synthesized using a straightforward one-step electrodeposition strategy. The actual Fe/Co molar ratios in the Fe_x-Co_y/NF samples were precisely determined through inductively coupled plasma mass spectrometry (ICP-MS) analysis (Table S1). The results revealed that the actual molar ratios of $Fe_{9.5}$-$Co_{0.5}$, Fe_9-Co_1, Fe_8-Co_2 and Fe_4-Co_6 were 12.0:1, 7.2:1, 3.1:1 and 2.7:4.7, respectively, slightly deviating from the theoretical ratios due to potential positional variations during the electrodeposition process. Additionally, a noticeable increase in the mass and percentage of Co was observed. The net weight of Fe-a/NF (a=5, 10, 20, 30 min) and Fe_x-Co_y/NF (x+y= 0.1 mol L^{-1}) samples before and after a 10-minute electrodeposition is detailed in Table S2.

X-ray diffraction (XRD) was employed to affirm the crystalline structure of the synthesized catalysts. As depicted in Fig. 1a, the XRD pattern of Fe species corresponds to the standard models of FeOOH (JCPDS: 29–0713) and $Fe(OH)_3$ (JCPDS: 38–0032) [26,27], while the XRD pattern of Co species primarily matches with $Co(OH)_2$ (JCPDS: 30–0443) [28,29]. In addition, three weaker peaks at 61.7°, 68.2° and 69.2° can be attributed to the (1 0 7), (0 1 8) and (1 1 3) plane of CoOOH (JCPDS: 14–0673) [30]. The XRD pattern of Fe_9-Co_1 species indicates that the peaks align predominantly with those observed in the Fe species, while the Co peaks exhibit relatively weaker intensities, attributable to the lower Co content in the Fe_9-Co_1 composition. Scanning electron microscopy (SEM) images of iron species grown on NF via electrodeposition at different time intervals are shown in Fig. S2. Fe-5/NF exhibits an intertwined sheet-like morphology, while Fe-10/NF, Fe-20/NF, and Fe-30/NF display flower-like structures with varying densities. Generally, pure iron species obtained through the electrodeposition process predominantly exhibit a nanoflower-flake morphology, differing in density and stacking arrangement. SEM images in Fig. S3 show Fe_x-Co_y/NF obtained through a 10-min electrodeposition process. At lower Co content, both Fe and $Fe_{9.5}$-$Co_{0.5}$ display flower-like structure morphologies. As the Co content increases, Fe_8-Co_2, Fe_4-Co_6, and Co morphologies transform into distinctive nanosheet-like structures. Fe_9-Co_1 showcases a thinner nanoflower morphology (Fig. 1b), which is favorable for exposing more active sites [31], and enhancing the interface between the electrode material and electrolyte, thereby ultimately improving catalytic performance. The transmission electron morphology (TEM) image (Fig. 1c) confirms the nano-flower morphology of Fe_9-Co_1. High-resolution TEM (HR-TEM) images reveal interplanar spacings of approximately 0.224 nm and 0.332 nm, corresponding to the (1 2 1) and (1 2 0) planes of FeOOH, respectively. Moreover, lattice stripes of 0.285 nm are associated with the (1 0 0) plane of $Co(OH)_2$ (Fig. 1d). These results provide further evidence that Fe_9-Co_1 primarily consists of FeOOH with a small amount of $Co(OH)_2$. Furthermore, energy-dispersive X-ray spectroscopy (EDS) (Fig. S4), high-angle circular dark-field scanning TEM (HAADF-STEM) images, and corresponding elemental mappings (Fig. 1e) verify the uniform distribution of Fe, O, and Co elements within the Fe_9-Co_1 nanoflowers.

X-ray photoelectron spectroscopy (XPS) provided further insight into the valence states and elemental composition of Fe_9-Co_1, Co and Fe species. As shown in Fig. S5, the XPS survey spectra reveal the presence of Fe, Co, and O elements, consistent with the TEM results. The high-resolution C 1 s spectrum was deconvoluted into three distinct peaks corresponding to C—C (284.8 eV), C—O (286.0 eV), and C═O (287.8 eV), respectively [32]. The binding energy based on C 1 s served as the calibration standard in this work (Fig. S6) [33]. The high-resolution Co 2p spectra of Fe_9-Co_1 and Co species are illustrated in Fig. 2a. The peaks at 780.9 eV and 782.6 eV can be attributed to Co(II) in $Co(OH)_2$ and Co (III) in CoOOH, respectively [34,35], accompanied with two satellite peaks. Simultaneously, the Fe 2p deconvolution peaks at 709.6 and 722.7 eV are assigned to Fe(II) in $Fe(OH)_2$, while 711.9 and 725.0 eV are attributed to Fe^{3+} (Fig. 2b), respectively [36,37]. To ensure accuracy, we performed three iterations of XPS data fitting and included error estimates in Fig. 2c-d. The CoOOH content in Fe_9-Co_1 species (42 %) was observed to be higher than that in pure Co (28 %). Additionally, the Fe_9-

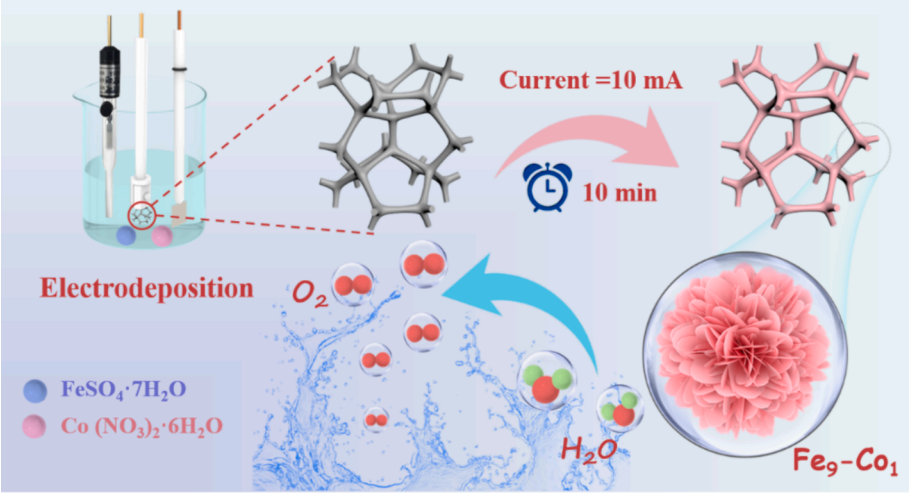

Scheme 1. Schematic illustration of the synthetic process of Fe_9-Co_1.

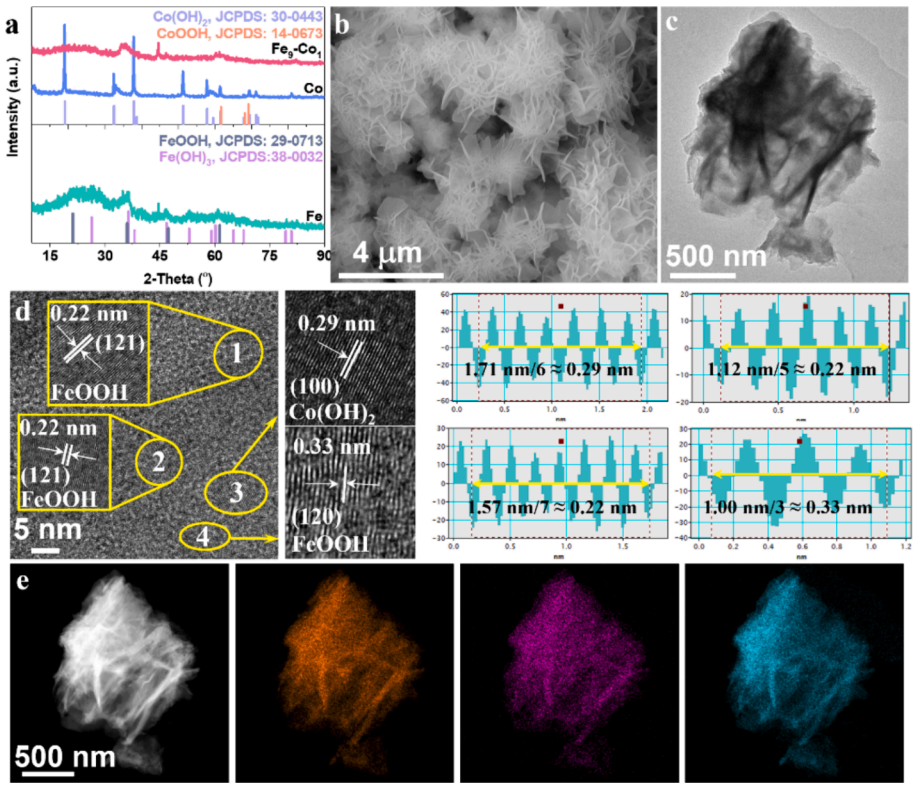

Fig. 1. (a) XRD patterns of Fe_9-Co_1, Fe, and Co species. (b) SEM image, (c) TEM image, (d) HR-TEM image and the corresponding lattice spacing profiles of the dotted line regions, and (e) HAADF-STEM image and corresponding element mappings of Fe_9-Co_1.

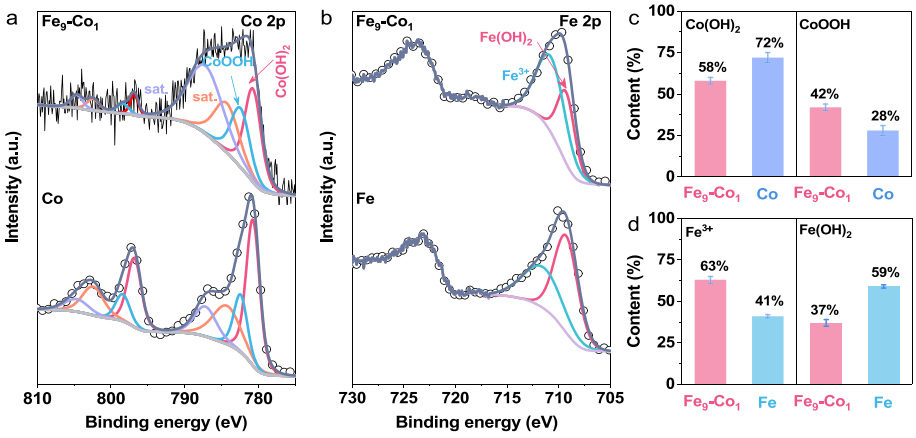

Fig. 2. High-resolution XPS survey spectra of (a) Co 2p, (b) Fe 2p of Fe_9-Co_1, Co and Fe species. (c-d) Percentage of different components in Fe_9-Co_1, Co and Fe.

Co_1 species exhibited a FeOOH content of approximately 63 %, exceeding that observed in the Fe species (around 41 %). This suggests that FeOOH and amorphous CoOOH may serve as the primary active sites, playing a pivotal role in enhancing the OER process [38].

3.2. Electrocatalytic performance in alkaline media

We expanded our investigation to assess the effects of electrodeposition time and various Fe/Co ratios on catalyst structure and properties. Initially, we explored the influence of morphology on catalytic performance by varying electrodeposition times. Shorter times resulted in fewer nanosheets and higher overpotentials, while longer times led to densely stacked structures and reduced performance (Fig. S7). Consequently, the Fe-10/NF displays the highest electrocatalytic activity among all the Fe-a/NF catalysts, with an overpotential of 244 mV at a current density of 50 mA cm^{-2}, surpassing Fe-5/NF (283 mV), Fe-20/NF (247 mV), Fe-30/NF (268 mV), and pure NF (518 mV). Subsequently, the OER polarization curves of samples with different Fe/Co ratios were evaluated (Fig. 3a). Fe_9-Co_1/NF exhibits the best OER activity, with a driving current density of 50 mA cm^{-2} at an overpotential of 222 mV. This is lower than Fe (277 mV), $Fe_{9.5}$-$Co_{0.5}$ (230 mV), Fe_8-Co_2 (239 mV), Fe_4-Co_6 (261 mV), Co (330 mV), and RuO_2 (240 mV), underscoring the advantages of higher hydroxyl iron (cobalt) oxide content and thinner nanosheets in Fe_9-Co_1, which facilitate the exposure of active sites and enhance catalytic performance. Specifically, Fe_9-Co_1 also demonstrates favorable OER kinetics with a Tafel slope of 43 mV dec^{-1} (Fig. 3b), surpassing Fe (47 mV dec^{-1}), $Fe_{9.5}$-$Co_{0.5}$ (47 mV dec^{-1}), Fe_8-Co_2 (48 mV dec^{-1}), Fe_4-Co_6 (58 mV dec^{-1}), Co (80 mV dec^{-1}) and RuO_2 (55 mV dec^{-1}). This indicates that Fe_9-Co_1 undergoes rapid OER kinetics [39]. Additionally, performance data for catalysts obtained through

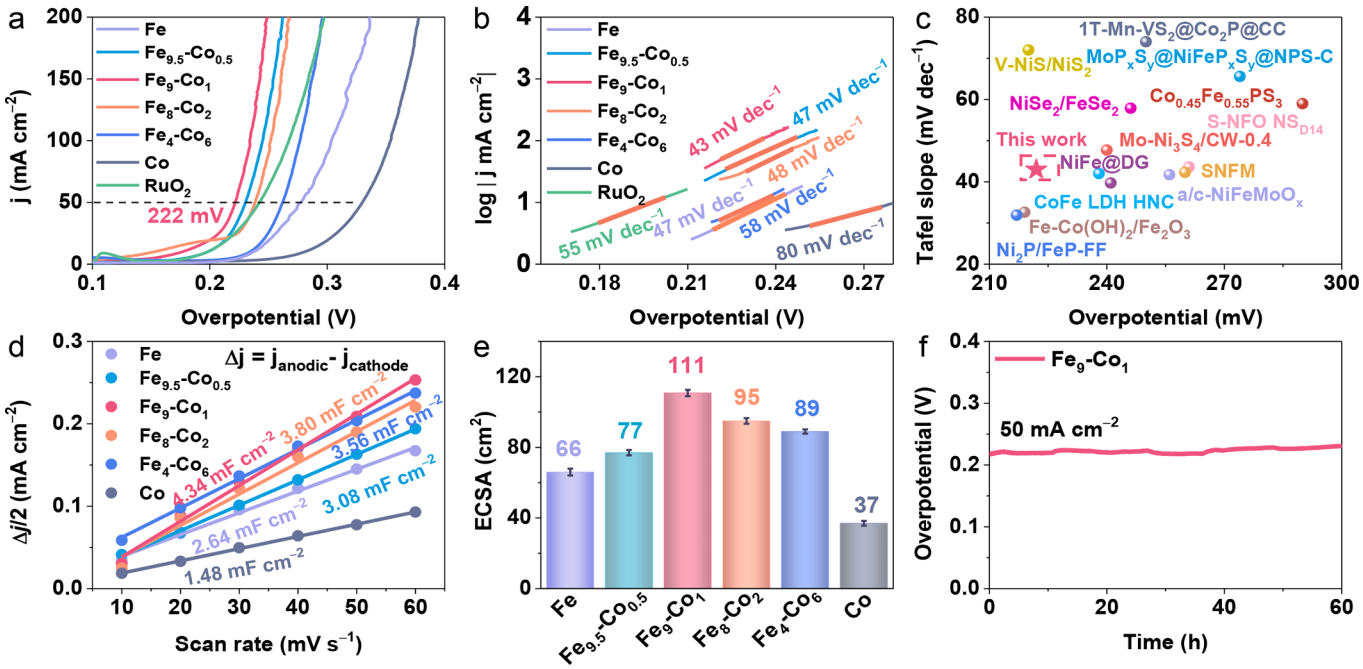

Fig. 3. OER performance of different electrocatalysts in 1.0 M KOH solution. (a) LSV polarization curves, and (b) corresponding Tafel slopes. (c) Comparison with the overpotentials and Tafel slopes of recently reported catalysts for OER activity at 10 mA cm^{-2}. (d) Double layer capacitance (C_{dl}). (e) Electrochemical active surface areas (ECSA). (f) Chronopotentiometry test of Fe$_9$-Co$_1$ at 50 mA cm^{-2}.

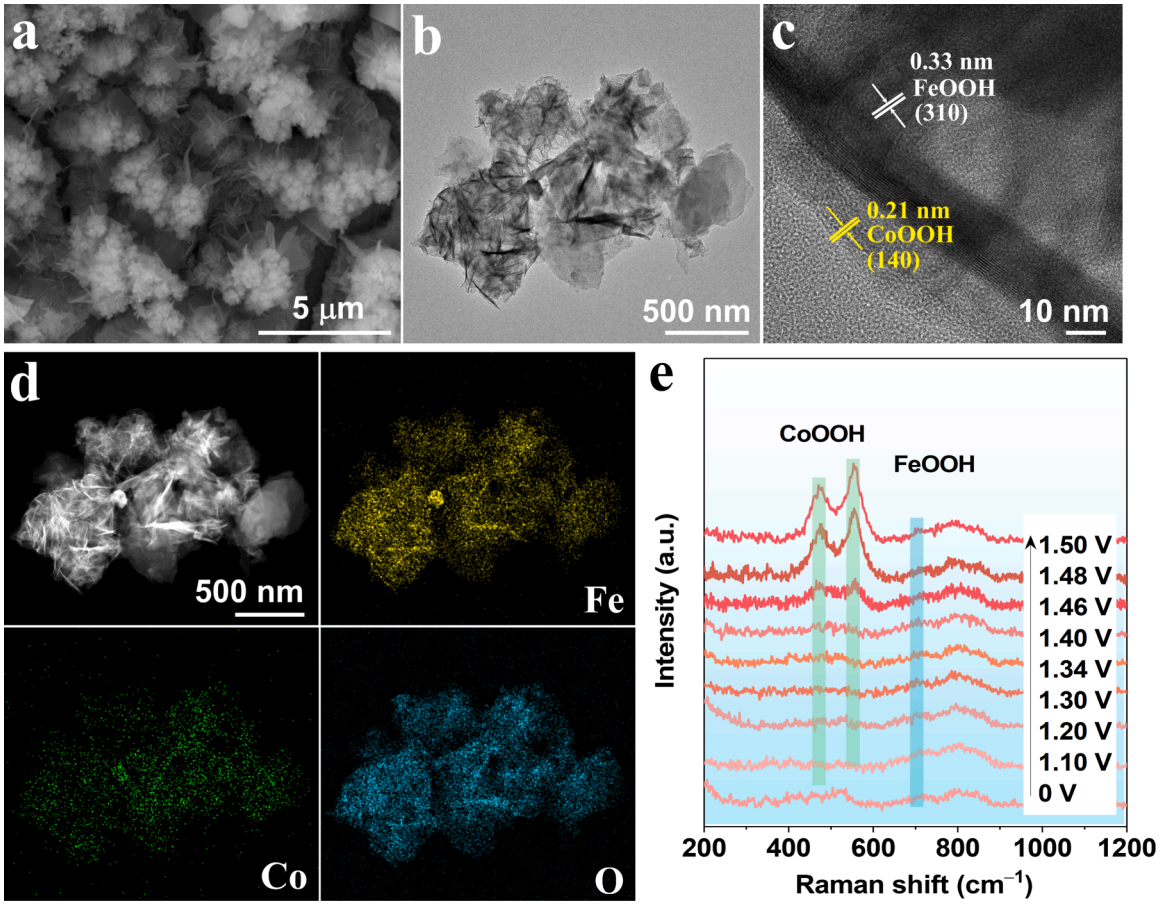

Fig. 4. (a) SEM image, (b) TEM image, (c) HR-TEM image, and (d) HAADF-STEM image and corresponding element mappings of Fe$_9$-Co$_1$ after long-term stability test in 1.0 M KOH solution. (e) In-situ Raman spectra of Fe$_9$-Co$_1$ at different potential ranges (V vs. RHE) in 1.0 M KOH.

electrodeposition of Fe species over different durations and Fe/Co molar ratios were provided in Table S3-S4. Moreover, Fe_9-Co_1 showcases exceptional electrochemical performance, rivaling and even surpassing recently reported OER electrocatalysts (Fig. 3c and Table S5). Electrochemical impedance spectroscopy (EIS) provides valuable insights into the interfacial charge transfer rate of catalysts [40]. Fe_9-Co_1 exhibits the lowest charge transfer resistance (R_{ct}) of 1.1 Ω, significantly lower than that of $Fe_{9.5}$-$Co_{0.5}$ (1.2 Ω), Fe_8-Co_2 (2.3 Ω), Fe_4-Co_6 (6.8 Ω), Fe (2.9 Ω), Co (34.0 Ω), and RuO_2 (1.6 Ω), indicating its incredible electrical conductivity and fast charge transfer ability (Fig. S8) [41]. Moreover, we evaluated the OER performance under varying pH conditions and observed that higher pH levels correlated with enhanced performance (Fig. S9). To gain a deeper understanding of the enhanced OER activity, cyclic voltammetry (CV) measurements were conducted to determine the electric double-layer capacitance (C_{dl}) (Figs. S10-11), enabling a more comprehensive investigation of the ECSA [42]. Fe_9-Co_1 supplies the largest C_{dl} value of 4.34 mF cm^{-2} among the compared catalysts (Fig. 3d). Moreover, Fe_9-Co_1 demonstrated a splendid ECSA value of 110.8 cm^2, signifying the greater exposure of active sites by the nanoflower morphology (Fig. 3e) [43,44]. This enhances mass transfer efficiency and contributes to improved performance [45,46]. Long-term stability is crucial for catalysts in practical applications. To evaluate the durability of Fe_9-Co_1 in a 1.0 M KOH solution, a stability test was performed at a current density of 50 mA cm^{-2}. Moreover, Fe_9-Co_1 exhibited minimal potential variation over approximately 60 h of continuous operation, contrasting with the notable decline observed in the other control samples (Fig. S12), demonstrating its robust durability (Fig. 3f).

After the OER stability test of Fe_9-Co_1, SEM, TEM, and XPS were employed to characterize the morphology and surface chemical states. The SEM and TEM results demonstrated the preserved integrity of the catalyst's nanoflower structure (Fig. 4a-b). HR-TEM analysis indicates that distinct lattice fringes correspond to the (3 1 0) plane of FeOOH after the OER stability test, while $Co(OH)_2$ is transformed to the high valence state of CoOOH (Fig. 4c). The corresponding element mappings elucidated the uniform distribution of Fe, Co, and O elements (Fig. 4d). Moreover, a slight change in the chemical composition is observed on the catalyst surface, with an increase in CoOOH content. The Fe XPS spectrum displays a prominent peak, signifying a complete conversion to Fe^{3+} ascribed to FeOOH, corroborating previous literature reports (Fig. S13) [15]. To elucidate the OER mechanism of the Fe_9-Co_1 catalyst, we performed in-situ Raman spectroscopy in a 1 M KOH solution at various applied potentials ranging from 0 to 1.5 V, as illustrated in Fig. 4e. As the applied potential increases, the prominent peaks emerge at 473 and 554 cm^{-1}, attributed to CoOOH when the potential reaches 1.40 V [47]. Furthermore, the characteristic peak corresponding to FeOOH at 709 cm^{-1} exhibited a progressive increase in intensity. These observations affirm CoOOH and FeOOH as the active sites during the electrochemical OER process, emphasizing the vital role of synergistic interaction between Co^{3+} and Fe^{3+} facilitating activity sites during the OER process [48].

Considering the admirable OER performance of Fe_9-Co_1, a two-electrode OWS device was assembled with Fe_9-Co_1 as the anode and Pt/C as the cathode, as illustrated in Fig. 5a. As anticipated, the Fe_9-

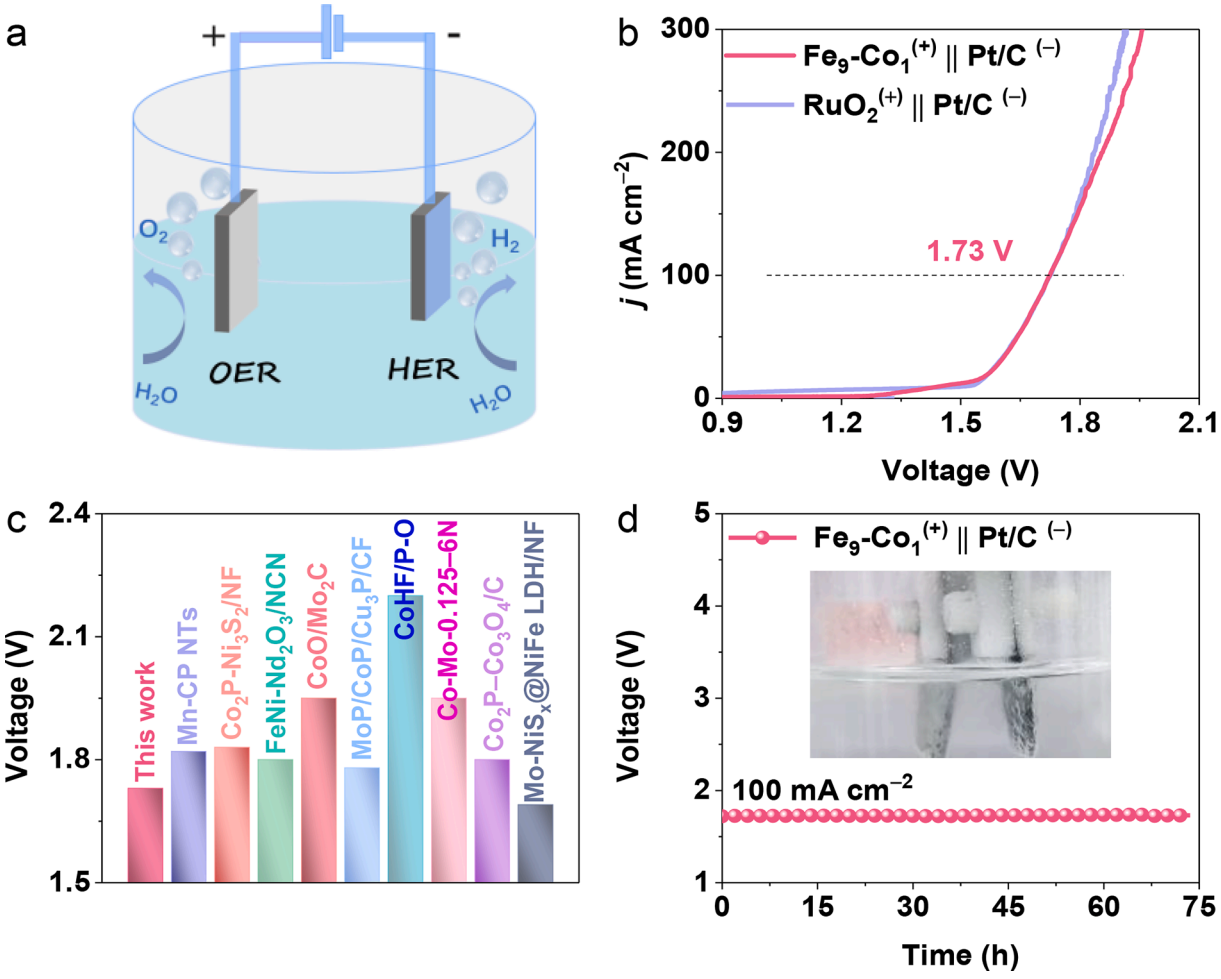

Fig. 5. (a) Schematic diagram of OWS electrolyzer. (b) LSV curves of Fe_9-$Co_1^{(+)}$||Pt/C $^{(-)}$ and the $RuO_2^{(+)}$||Pt-$C^{(-)}$ for OWS in 1.0 M KOH. (c) Comparison the cell voltage at 100 mA cm^{-2} with previously reported catalysts in 1.0 M KOH. (d) Long-term stability test of Fe_9-$Co_1^{(+)}$||Pt/$C^{(-)}$ at 10 mA cm^{-2}.

$Co_1^{(+)}||Pt/C^{(-)}$ achieved a current density of 100 mA cm^{-2} at a low voltage of 1.73 V, surpassing the performance of $RuO_2^{(+)}||Pt/C^{(-)}$ (Fig. 5b), as well as many other reported catalysts (Fig. 5c and Table S6). Furthermore, a stability test was conducted to verify the practical applicability of the Fe_9-Co_1 catalyst. As depicted in Fig. 5d, the Fe_9-Co_1 catalyst manifested negligible degradation even after continuous operation for over 70 h at a current density of 10 mA cm^{-2}. These results not only confirm the enhanced stability and durability of the Fe_9-Co_1 catalyst but also emphasize its significant potential in enabling highly efficient catalytic OWS.

Briefly, the excellent OER performance and stability of Fe_9-Co_1 in an alkaline electrolyte can be attributed to several key factors: (i) The highly active FeOOH/CoOOH were identified as the true active sites, and the synergistic interaction between Fe and Co components effectively reduces the energy barriers between the active sites and oxygen-containing intermediates, leading to enhanced catalytic activity [49–51]. (ii) The construction of nanoflower structures significantly increase the specific surface area, providing an abundance of conductive channels for active substance diffusion, electron transfer, and efficient mass transport [52,53]. (iii) The fabrication of 3D self-supporting electrode plays a pivotal role in reducing electrode resistance, effectively expediting the electron transfer process [54].

4. Conclusions

In summary, a facile one-step electrodeposition method was successfully employed to synthesize Fe/Co hydro(oxy)oxides composites. The morphology and properties of the catalysts were further tailored by precisely adjusting the Fe/Co ratio (Fe_x-Co_y). The optimized Fe_9-Co_1 catalyst showcases a progressive OER catalytic performance, achieving a low overpotential of 222 mV at 50 mA cm^{-2}, exceeding the performance of most recently reported non-precious metal catalysts. Additionally, it exhibits robust stability, with no observable degradation observed for over 60 h at 10 mA cm^{-2}. Furthermore, the assembled Fe_9-$Co_1^{(+)}||Pt/C^{(-)}$ electrolyzer achieves a current density of 100 mA cm^{-2} at a low voltage of 1.73 V, comparable to that of the benchmark $RuO_2^{(+)}||Pt/C^{(-)}$ system. The good catalytic performance of Fe_9-Co_1 is likely attributed to its distinctive nanoflower morphology, which facilitates enhanced exposure of active sites. TEM, XPS, and in-situ Raman analyses validate the transition of Fe_9-Co_1 to the high valence state CoOOH/FeOOH as the active catalytic centers, contributing to the observed OER performance. This work introduces a facile approach for synthesizing efficient OER electrocatalysts, highlighting the importance of the high-valence state of Fe/Co as the active site during the OER process.

CRediT authorship contribution statement

Lixia Wang: Writing – original draft, Data curation, Conceptualization. **Jia Huang:** Methodology, Data curation. **Qiuping Gan:** Investigation. **Jiasui Huang:** Formal analysis. **Xinran Hu:** Investigation. **Dongcheng Liu:** Writing – review & editing. **Tayirjan Taylor Isimjan:** Writing – review & editing. **Xiulin Yang:** Writing – review & editing, Supervision, Funding acquisition.

Declaration of competing interest

The authors declare that they have no known competing financial interests or personal relationships that could have appeared to influence the work reported in this paper.

Data availability

Data will be made available on request.

Acknowledgements

This work has been supported by the National Natural Science Foundation of China (no. 52363028, 21965005), Natural Science Foundation of Guangxi Province (2021GXNSFAA076001, 2018GXNSFAA294077), Guangxi Technology Base and Talent Subject (GUIKE AD23023004, GUIKE AD20297039).

Appendix A. Supplementary data

Supplementary data to this article can be found online at https://doi.org/10.1016/j.jcis.2024.05.034.

References

[1] Z. Wu, Y. Wang, D. Liu, B. Zhou, P. Yang, R. Liu, W. Xiao, T. Ma, J. Wang, L. Wang, Hexagonal Defect-Rich MnO_x/RuO_2 with Abundant Heterointerface to Modulate Electronic Structure for Acidic Oxygen Evolution Reaction, Adv. Funct. Mater. 33 (2023) 2307010, https://doi.org/10.1002/adfm.202307010.
[2] L. Wang, J. Huang, Z. Huang, H. Li, T. Taylor Isimjan, X. Yang, Revealing dynamic structural evolution of V and P co-doping-induced Co defects as large-current water oxidation catalyst, Chem. Eng. J. 472 (2023) 144924, https://doi.org/10.1016/j.cej.2023.144924.
[3] S. Xu, P. Zhang, R. Zhao, J. Wook Bae, H. Li, J. Yong Lee, P.J. Yoo, Engineered oxidation states in $NiCo_2O_4$@CeO_2 nanourchin architectures with abundant oxygen vacancies for enhanced oxygen evolution reaction performance, Chem. Eng. J. 482 (2024) 148787, https://doi.org/10.1016/j.cej.2024.148787.
[4] K. Saini, A.N. Nair, A. Yadav, L.G. Enriquez, C.J. Pollock, S.D. House, S. Yang, X. Guo, S.T. Sreenivasan, Nickel-Based Single-Molecule Catalysts with Synergistic Geometric Transition and Magnetic Field-Assisted Spin Selection Outperform RuO_2 for Oxygen Evolution, Adv. Energy Mater. 13 (2023) 2302170, https://doi.org/10.1002/aenm.202302170.
[5] H. Jia, N. Yao, J. Zhu, Y. Liu, Y. Lao, H. Cong, W. Luo, Ni_3N Modified MOF Heterostructure with Tailored Electronic Structure for Efficient Overall Water Splitting, Chin. J. Struct. Chem. 41 (2022) 2208031–2208036, https://doi.org/10.14102/j.cnki.0254-5861.2022-0112.
[6] C.-F. Li, L.-J. Xie, J.-W. Zhao, L.-F. Gu, H.-B. Tang, L. Zheng, G.-R. Li, Interfacial Fe−O−Ni−O−Fe Bonding Regulates the Active Ni Sites of Ni-MOFs via Iron Doping and Decorating with FeOOH for Super-Efficient Oxygen Evolution, Angew. Chem. Int. Ed. 61 (2022) e202116934, https://doi.org/10.1002/anie.202116934.
[7] Z. An, H. Xue, J. Sun, N. Guo, T. Song, J. Sun, Y.-R. Hao, Q. Wang, Co-Construction of Sulfur Vacancies and Heterogeneous Interface into Ni_3S_2/MoS_2 Catalysts to Achieve Highly Efficient Overall Water Splitting, Chin. J. Struct. Chem. 41 (2022) 2208037–2208043, https://doi.org/10.14102/j.cnki.0254-5861.2022-0130.
[8] J. Baek, M.D. Hossain, P. Mukherjee, J. Lee, K.T. Winther, J. Leem, Y. Jiang, W. C. Chueh, M. Bajdich, X. Zheng, Synergistic effects of mixing and strain in high entropy spinel oxides for oxygen evolution reaction, Nat. Commun. 14 (2023) 5936, https://doi.org/10.1038/s41467-023-41359-7.
[9] N. Chen, S. Che, Y. Yuan, H. Liu, N. Ta, G. Li, F.J. Chen, G. Ma, B. Jiang, N. Wu, W. Yu, F. Yang, Y. Li, Self-supporting electrocatalyst constructed from in-situ transformation of $Co(OH)_2$ to metal-organic framework to Co/CoP/NC nanosheets for high-current-density water splitting, J. Colloid Interface Sci. 645 (2023) 513–524, https://doi.org/10.1016/j.jcis.2023.04.089.
[10] S. Li, Y. Gao, N. Li, L. Ge, X. Bu, P. Feng, Transition metal-based bimetallic MOFs and MOF-derived catalysts for electrochemical oxygen evolution reaction, Energy Environ. Sci. 14 (2021) 1897–1927, https://doi.org/10.1039/D0EE03697H.
[11] X.-Y. Zhang, F.-T. Li, Y.-W. Dong, B. Dong, F.-N. Dai, C.-G. Liu, Y.-M. Chai, Dynamic anion regulation to construct S-doped FeOOH realizing 1000 mA cm^{-2}-level-current-density oxygen evolution over 1000 h, Appl. Catal. B Environ. 315 (2022) 121571, https://doi.org/10.1016/j.apcatb.2022.121571.
[12] R. Li, Y. Wang, B. Chen, H. Zhang, C. Yan, X. Xu, M. Humayun, D.P. Debecker, C. Wang, Core-shell structured Co(OH)F@FeOOH enables highly efficient overall water splitting in alkaline electrolyte, Int. J. Hydrogen Energy 51 (2023) 1292–1302, https://doi.org/10.1016/j.ijhydene.2023.07.254.
[13] L. Li, Z. Wang, X. She, L. Pan, C. Xi, D. Wang, J. Yi, J. Yang, Ni-modified FeOOH integrated electrode by self-source corrosion of nickel foam for high-efficiency electrochemical water oxidation, J. Colloid Interface Sci. 652 (2023) 789–797, https://doi.org/10.1016/j.jcis.2023.08.112.
[14] X. Han, C. Yu, J. Yang, X. Song, C. Zhao, S. Li, Y. Zhang, H. Huang, Z. Liu, H. Huang, X. Tan, J. Qiu, Electrochemically Driven Coordination Tuning of FeOOH Integrated on Carbon Fiber Paper for Enhanced Oxygen Evolution, Small 15 (2019) 1901015, https://doi.org/10.1002/smll.201901015.
[15] Z. Zang, Y. Ren, X. Li, Y. Cheng, L. Li, X. Yu, X. Yang, Z. Lu, X. Zhang, H. Liu, Interfacial microenvironment regulation of FeOOH/S-Co heterostructure catalysts via S atoms for overall water splitting, J. Mater. Chem. A 11 (2023) 24618–24628, https://doi.org/10.1039/D3TA05613A.
[16] J. Cheng, B. Shen, Y. Song, J. Liu, Q. Ye, M. Mao, Y. Cheng, FeOOH decorated CoP porous nanofiber for enhanced oxygen evolution activity, Chem. Eng. J. 428 (2022) 131130, https://doi.org/10.1016/j.cej.2021.131130.
[17] Y. Wang, Y. He, M. Zhou, Fabrication of hierarchical $Co(OH)_2$@$Ni(OH)_2$ core-shell nanosheets on carbon cloth as an advanced electrocatalyst for oxygen evolution

reaction, Appl. Surf. Sci. 479 (2019) 1270–1276, https://doi.org/10.1016/j.apsusc.2019.02.170.
[18] L.-F. Gu, C.-F. Li, J.-W. Zhao, L.-J. Xie, J.-Q. Wu, Q. Ren, G.-R. Li, Dual modulation of lattice strain and charge polarization induced by $Co(OH)_2/Ni(OH)_2$ interfaces for efficient oxygen evolution catalysis, J. Mater. Chem. A 9 (2021) 13279–13287, https://doi.org/10.1039/D1TA01866C.
[19] K. Guo, J. Jia, X. Lu, S. Wang, H. Wang, H. Wu, C. Xu, F-doped NiOOH Derived from Progressive Reconstruction for Efficient and Durable Water Oxidation, Inorg. Chem. Front. 11 (2024) 1479–1491, https://doi.org/10.1039/D3QI02619A.
[20] S. Zhang, Z. Huang, T.T. Isimjan, D. Cai, X. Yang, Accurately substituting Fe for Ni_2 atom in Ni-MOF with defect-rich for efficient oxygen evolution reaction: Electronic reconfiguration and mechanistic study, Appl. Catal. B Environ. 343 (2024) 123448, https://doi.org/10.1016/j.apcatb.2023.123448.
[21] D. Li, R. Xiang, F. Yu, J. Zeng, Y. Zhang, W. Zhou, L. Liao, Y. Zhang, D. Tang, H. Zhou, In Situ Regulating Cobalt/Iron Oxide-Oxyhydroxide Exchange by Dynamic Iron Incorporation for Robust Oxygen Evolution at Large Current Density, Adv. Mater. 36 (2023) 2305685, https://doi.org/10.1002/adma.202305685.
[22] Y. Wang, C. Yang, Z. Li, Z. Liang, G. Cao, The NH_x Group Induced Formation of 3D α-$Co(OH)_2$ Curly Nanosheet Aggregates as Efficient Oxygen Evolution Electrocatalysts, Small 16 (2020) 2001973, https://doi.org/10.1002/smll.202001973.
[23] B. Guo, H. Huo, Q. Zhuang, X. Ren, X. Wen, B. Yang, X. Huang, Q. Chang, S. Li, Iron Oxyhydroxide: Structure and Applications in Electrocatalytic Oxygen Evolution Reaction, Adv. Funct. Mater. 33 (2023) 2300557, https://doi.org/10.1002/adfm.202300557.
[24] J. Li, Y. Kang, Z. Lei, P. Liu, Well-controlled 3D flower-like $CoP_3/CeO_2/C$ heterostructures as bifunctional oxygen electrocatalysts for rechargeable Zn-air batteries, Appl. Catal. B Environ. 321 (2023) 122029, https://doi.org/10.1016/j.apcatb.2022.122029.
[25] Y.-N. Zhou, R.-Y. Fan, S.-Y. Dou, B. Dong, Y. Ma, W.-L. Yu, M.-X. Li, Y.-L. Zhou, C.-G. Liu, Y.-M. Chai, Tailoring electron transfer with Ce integration in ultrathin Co $(OH)_2$ nanosheets by fast microwave for oxygen evolution reaction, J. Energy Chem. 59 (2021) 299–305, https://doi.org/10.1016/j.jechem.2020.10.037.
[26] S. Wu, J. Lu, Z. Ding, N. Li, F. Fu, B. Tang, Cr(vi) removal by mesoporous FeOOH polymorphs: performance and mechanism, RSC Adv. 6 (2016) 82118–82130, https://doi.org/10.1039/C6RA14522A.
[27] J. Fei, J. Zhao, C. Du, H. Ma, H. Zhang, J. Li, The facile 3D self-assembly of porous iron hydroxide and oxide hierarchical nanostructures for removing dyes from wastewater, J. Mater. Chem. A 1 (2013) 10300–10305, https://doi.org/10.1039/C3TA11938F.
[28] S. Wan, J. Qi, W. Zhang, W. Wang, S. Zhang, K. Liu, H. Zheng, J. Sun, S. Wang, R. Cao, Hierarchical Co(OH)F Superstructure Built by Low-Dimensional Substructures for Electrocatalytic Water Oxidation, Adv. Mater. 29 (2017) 1700286, https://doi.org/10.1002/adma.201700286.
[29] J. Liu, J. Nai, T. You, P. An, J. Zhang, G. Ma, X. Niu, C. Liang, S. Yang, L. Guo, The Flexibility of an Amorphous Cobalt Hydroxide Nanomaterial Promotes the Electrocatalysis of Oxygen Evolution Reaction, Small 14 (2018) 1703514, https://doi.org/10.1002/smll.201703514.
[30] X. Feng, W. Xing, L. Song, Y. Hu, In situ synthesis of a MoS_2/CoOOH hybrid by a facile wet chemical method and the catalytic oxidation of CO in epoxy resin during decomposition, J. Mater. Chem. A 2 (2014) 13299–13308, https://doi.org/10.1039/C4TA01885K.
[31] Z.-H. Zhang, Z.-R. Yu, Y. Zhang, A. Barras, A. Addad, P. Roussel, L.-C. Tang, M. Naushad, S. Szunerits, R. Boukherroub, Construction of desert rose flower-shaped NiFe LDH-Ni_3S_2 heterostructures via seawater corrosion engineering for efficient water-urea splitting and seawater utilization, J. Mater. Chem. A 11 (2023) 19578–19590, https://doi.org/10.1039/D3TA02770H.
[32] C. Hu, F. Wei, Q. Liang, Q. Peng, Y. Yang, T. Taylor Isimjan, X. Yang, Electronically modulated d-band centers of MOF-derived carbon-supported Ru/HfO_2 for oxygen reduction and aqueous/flexible zinc-air batteries, J. Energy Chem. 80 (2023) 247–255, https://doi.org/10.1016/j.jechem.2023.01.047.
[33] L. Wang, Y. Qin, H. Li, Z. Huang, M. Gao, T.T. Isimjan, X. Yang, Oxygen vacancy engineering of mesoporous Bi-Fe_2O_3@NC multi-channel microspheres for remarkable oxygen reduction and aqueous/flexible Zn-air batteries, J. Colloid Interface Sci. 650 (2023) 719–727, https://doi.org/10.1016/j.jcis.2023.07.033.
[34] W.-J. Liu, X. Hu, H.-C. Li, H.-Q. Yu, Pseudocapacitive Ni-Co-Fe Hydroxides/N-Doped Carbon Nanoplates-Based Electrocatalyst for Efficient Oxygen Evolution, Small 14 (2018) 1801878, https://doi.org/10.1002/smll.201801878.
[35] X. Xu, Z. Zhong, X. Yan, L. Kang, J. Yao, Cobalt layered double hydroxide nanosheets synthesized in water–methanol solution as oxygen evolution electrocatalysts, J. Mater. Chem. A 6 (2018) 5999–6006, https://doi.org/10.1039/C7TA10351D.
[36] S. Anantharaj, K. Karthick, M. Venkatesh, T.V.S.V. Simha, A.S. Salunke, L. Ma, H. Liang, S. Kundu, Enhancing electrocatalytic total water splitting at few layer Pt-NiFe layered double hydroxide interfaces, Nano Energy 39 (2017) 30–43, https://doi.org/10.1016/j.nanoen.2017.06.027.
[37] Z. Li, L. Liu, A. Jiménez González, D.-Y. Wang, Bioinspired polydopamine-induced assembly of ultrafine $Fe(OH)_3$ nanoparticles on halloysite toward highly efficient fire retardancy of epoxy resin via an action of interfacial catalysis, Polym. Chem. 8 (2017) 3926–3936, https://doi.org/10.1039/C7PY00660H.
[38] S. Mondal, M. Riyaz, D. Bagchi, N. Dutta, A.K. Singh, C.P. Vinod, S.C. Peter, Distortion-Induced Interfacial Charge Transfer at Single Cobalt Atom Secured on Ordered Intermetallic Surface Enhances Pure Oxygen Production, ACS Nano 17 (2023) 23169–23180, https://doi.org/10.1021/acsnano.3c09680.
[39] D. Xu, S. Liu, M. Zhang, L. Xu, H. Gao, J. Yao, Manipulating the Dynamic Self-Reconstruction of CoP Electrocatalyst Driven by Charge Transport and Ion Leaching, Small 19 (2023) 2300201, https://doi.org/10.1002/smll.202300201.
[40] H. Su, S. Song, N. Li, Y. Gao, P. Li, L. Ge, T. Ma, Flexibility Tuning of Dual-Metal S—Fe—Co—N_5 Catalysts with O-Axial Ligand Structure for Electrocatalytic Water Splitting, Adv. Energy Mater. 13 (2023) 2301547, https://doi.org/10.1002/aenm.202301547.
[41] K. Wang, Y. Li, J. Hu, Z. Lu, J. Xie, A. Hao, Y. Cao, Deep reconstruction of transition metal molybdate@hydroxide heterostructure triggered by anion-exchange reaction as high efficiency water oxidation electrocatalyst, Chem. Eng. J. 447 (2022) 137540, https://doi.org/10.1016/j.cej.2022.137540.
[42] Y. Zhang, D. Ma, Y. Lei, T. Zhu, J. Hu, Y. Tang, Z. Chen, J. Huang, Y. Lai, Z. Lin, Markedly enhanced hydrogen production in wastewater via ammonia-mediated metal oxyhydroxides active sites on bifunctional electrocatalysts, Nano Energy 117 (2023) 108896, https://doi.org/10.1016/j.nanoen.2023.108896.
[43] X. Lin, X. Li, L. Shi, F. Ye, F. Liu, D. Liu, In Situ Electrochemical Restructuring B-Doped Metal–Organic Frameworks as Efficient OER Electrocatalysts for Stable Anion Exchange Membrane Water Electrolysis, Small 2308517 (2023), https://doi.org/10.1002/smll.202308517.
[44] X. Hou, T. Jiang, X. Xu, X. Wang, J. Zhou, H. Xie, Z. Liu, L. Chu, M. Huang, Coupling of NiFe-Based Metal-Organic Framework Nanosheet Arrays with Embedded Fe-Ni_3S_2 Clusters as Efficient Bifunctional Electrocatalysts for Overall Water Splitting, Chin. J. Struct. Chem. 41 (2022) 2207074–2207080, https://doi.org/10.14102/j.cnki.0254-5861.2022-0145.
[45] D. Zhang, H. Li, H. Lu, Z. Yin, Z. Fusco, A. Riaz, K. Reuter, K. Catchpole, S. Karuturi, Unlocking the performance of ternary metal (hydro)oxide amorphous catalysts via data-driven active-site engineering, Energy Environ. Sci. 16 (2023) 5065–5075, https://doi.org/10.1039/D3EE01981K.
[46] R.B. Ghising, U.N. Pan, M.R. Kandel, P.P. Dhakal, S. Sidra, D.H. Kim, N.H. Kim, J. H. Lee, Ruthenium single atoms implanted on NiS_2-FeS_2 nanosheet heterostructures for efficacious water electrolysis, J. Mater. Chem. A 12 (2024) 3489–3500, https://doi.org/10.1039/D3TA05630A.
[47] X. Yang, J. Cheng, Y. Xu, H. Li, W. Tu, J. Zhou, Heterogeneous ultra-thin FeCo-LDH@$Co(OH)_2$ nanosheets facilitated electrons transfer for oxygen evolution reaction, Chem. Eng. J. 472 (2023) 145076, https://doi.org/10.1016/j.cej.2023.145076.
[48] J. Zhu, J. Chen, X. Li, K. Luo, Z. Xiong, Z. Zhou, W. Zhu, Z. Luo, J. Huang, Y. Li, Steering surface reconstruction of hybrid metal oxides for efficient oxygen evolution reaction in water splitting and zinc-air batteries, J. Energy Chem. 92 (2024) 383–393, https://doi.org/10.1016/j.jechem.2024.01.020.
[49] M. Yang, J.-Y. Xie, W.-L. Yu, Y.-N. Cao, B. Dong, Y.-N. Zhou, F.-L. Wang, Q.-Z. Li, Y.-L. Zhou, Y.-M. Chai, Fe(Co)OOH Dynamically Stable Interface Based on Self-Sacrificial Reconstruction for Long-Term Electrochemical Water Oxidation, ACS Appl. Mater. Interfaces 13 (2021) 17450–17458, https://doi.org/10.1021/acsami.0c22620.
[50] L. Zhi, M. Zhang, J. Tu, M. Li, J. Liu, Coordination polymer and layered double hydroxide dual-precursors derived polymetallic phosphides confined in N-doped hierarchical porous carbon nanoflower as a highly efficient bifunctional electrocatalyst for overall water splitting, J. Colloid Interface Sci. 659 (2024) 82–93, https://doi.org/10.1016/j.jcis.2023.12.113.
[51] J.-X. Feng, H. Xu, Y.-T. Dong, S.-H. Ye, Y.-X. Tong, G.-R. Li, FeOOH/Co/FeOOH Hybrid Nanotube Arrays as High-Performance Electrocatalysts for the Oxygen Evolution Reaction, Angew. Chem. Int. Ed. 55 (2016) 3694–3698, https://doi.org/10.1002/anie.201511447.
[52] N. Chen, S. Che, H. Liu, G. Li, N. Ta, F. Jiang Chen, B. Jiang, N. Wu, Z. Li, W. Yu, F. Yang, Y. Li, Multistage interfacial engineering of 3D carbonaceous Ni_2P nanospheres/nanoflowers derived from Ni-BTC metal–organic frameworks for overall water splitting, J. Colloid Interface Sci. 638 (2023) 582–594, https://doi.org/10.1016/j.jcis.2023.02.003.
[53] X. Liu, S. Deng, P. Liu, J. Liang, M. Gong, C. Lai, Y. Lu, T. Zhao, D. Wang, Facile self-template fabrication of hierarchical nickel-cobalt phosphide hollow nanoflowers with enhanced hydrogen generation performance, Sci. Bull. 64 (2019) 1675–1684, https://doi.org/10.1016/j.scib.2019.09.014.
[54] H. Jiang, Y. Yu, X. Duan, P. Chen, S. Wang, X. Qiu, L. Ye, X. Tu, Heterostructured MoO_3 Anchored Defect-Rich NiFe-LDH/NF as a Robust Self-Supporting Electrocatalyst for Overall Water Splitting, Small 20 (2024) 2307797, https://doi.org/10.1002/smll.202307797.